Conditional Generative Modeling for Amorphous Multi-Element Materials

Honglin Li,[1,2,*] Chuhao Liu,[3,4,*] Yongfeng Guo,[5,*] Xiaoshan Luo,[1,*] Yijie Chen,[6,*] Guangsheng Liu,[7] Yu Li,[2] Ruoyu Wang,[8] Zhenyu Wang,[1] Jianzhuo Wu,[5] Cheng Ma,[1] Zhuohang Xie,[1] Jian Lv,[1] Yufei Ding,[9] Huabin Zhang,[10] Jian Luo,[2,7] Zhicheng Zhong,[8] Mufan Li,[4,†] Yanchao Wang,[1,‡] and Wan-Lu Li[2,7,§]

[1] *Key Laboratory of Material Simulation Methods and Software of Ministry of Education, College of Physics, Jilin University, Changchun, China*
[2] *Aiiso Yufeng Li Family Department of Chemical and Nano Engineering, University of California, San Diego, La Jolla, CA, USA*
[3] *Institute of Molecular Engineering Plus, College of Chemistry, Fuzhou University, Fuzhou, China*
[4] *College of Chemistry and Molecular Engineering, Peking University, Beijing, China*
[5] *School of Physics, Nankai University, Tianjin, China*
[6] *Institute of Modern Physics, Fudan University, Shanghai, China*
[7] *Program in Materials Science and Engineering, University of California, San Diego, La Jolla, CA, USA*
[8] *School of Artificial Intelligence and Data Science, University of Science and Technology of China, Hefei 230026, China*
[9] *Department of Computer Science and Engineering, University of California, San Diego, La Jolla, CA, USA*
[10] *Center for Renewable Energy and Storage Technologies, Physical Science and Engineering Division, King Abdullah University of Science and Technology, Thuwal, Kingdom of Saudi Arabia*

(Dated: March 19, 2025)

Contents

* These authors contribute equally to this work.
† mufanli@pku.edu.cn
‡ wyc@calypso.cn
§ wal019@ucsd.edu

S1 Supplementary Text

A. Normalized variance of PDM

To investigate the chemical short-range order of the structure, we first computed the variance of atomic pairs in the PDM across different energy ranges. This variance reflects the uniformity and consistency of atomic pair coordination within specific energy ranges. Specifically, atomic pairs with smaller variances exhibit better coordination consistency within a given energy range. Atomic pairs that retain smaller variances in low-energy regions are likely to play a significant role in the structural stability, while atomic pairs with larger variances demonstrate greater spatial dispersion and may contribute less to structural stability.

Actually, the variance of atomic pair coordination numbers is also correlated with their mean values. To simplify the comparison of the relative consistency of atomic pair coordination numbers, we use the variance-to-mean ratio for subsequent statistical analysis. For structures across all energy ranges, the variance-to-mean ratios of different atomic pairs are shown in fig. S1. Oxygen-oxygen pairs are excluded due to their significantly larger variance, which would affect the observation of other atom pairs.

PDM is classified into self-pair interactions, intermetallic pairs, and metal-oxygen interactions. The variance-to-mean ratio of the PDM in the energy ranges below and above -920 eV is shown in fig. S2. It can be observed that, regardless of whether the energy is less than or greater than -920 eV, the variance of self-pair interactions is always smaller than that of intermetallic pairs, which in turn is smaller than that of metal-oxygen pairs. However, the relative ordering of these three atomic pair groups varies across different energy ranges. For the more stable structures with energies below -920 eV, it is notable that some Ni-X pairs (such as Ni-Ni, Fe-Ni, and B-Ni), as well as B-B pairs, have relatively small coordination number variances, suggesting that these atomic pairs may play a crucial role in forming stable structures and significantly impact the chemical short-range order of the structure.

B. Cluster expansion analysis

The high compositional complexity of the system involving six elements presents significant challenges because of the intricate interactions and vast configurational space. In smaller atomic systems, atomic interactions may not be fully captured, and the enumeration of configurations becomes stagnant. As the number of atoms in the system up to six, the configurational space grows exponentially, complicating the structure search process. To address this challenge, we utilized a set of fixed-concentration disordered models constructed using the SQS structural relaxation method to provide input energies. A $3 \times 4 \times 5$ supercell containing 120 atoms was employed, and a total of 2,500 structures were considered in the analysis. As illustrated in fig. S3A, the fitted LOOCV scores persist at a high level (0.095 eV), exceeding the accuracy threshold suggested by ATAT (0.02 eV). Additionally, increasing the diameter of the two-body clusters or incorporating three-body clusters leads to an even higher CV score. For CE fitting, the two-body cluster with the lowest LOOCV score (cutoff = 5.5 Å) was selected and fitted using the least-squares method to obtain the ECI for further testing. Subsequent five-fold cross-validation performed with the scikit-learn method yielded a root mean squared error (RMSE) of approximately 0.09 eV, as shown in (fig. S3B). And the predicted energies (fig. S3C) exhibit poor agreement with an R^2 value of only 0.1, which is markedly lower than the typical accuracy achieved for alloys with crystalline structures. This poor fitting primarily arises from the significant displacement of non-metallic atoms during structural relaxation, which disrupts the BCC symmetry of the system, as depicted in fig. S3D–E. Therefore, for amorphous high-entropy materials with a substantial concentration of non-metallic atoms, accurately predicting lattice site occupancy and cluster energies using the CE method is challenging.

In addition to the least-squares fitting method, two additional fitting methods were also employed to test the cluster expansion based on the selected SQS structures. Fig. 5 shows the two-body cluster truncation radius tests for Lasso and Ridge fitting, with RMSE values for both methods exceeding 0.09 eV (fig. S4A–B).

Furthermore, by scanning the hyperparameter alpha for these two methods using the same two-body cluster truncation radius (5.5 Å) as the least squares fitting, it was found that the RMSE values converge near 0.1 eV (fig S4C–D), which is slightly higher than the least-squares fitting results via ATAT. Note that the Lasso and Ridge fitting were conducted using the ICET package [1]. Similar results obtained from these two additional methods indicate that their fitting performance is comparable to that of the least squares method, further suggesting that the amorphous high-entropy ceramic systems studied in this paper are not suitable for investigation via cluster expansion methods.

C. Diffusion rate analysis

The diffusion rate (D) can be inferred from the slope of the MSD curve, which can be calculated as:

$$\langle (r(t) - r(0))^2 \rangle = 6Dt \tag{S1}$$

As the boron content increases, the overall diffusion rate of the system decreases, as shown in fig. S5A. This trend is also observed for metal and boron species (Fig. 3C in the main text) and oxygen components (fig. S5B). Additionally, oxygen atoms exhibit higher diffusion rates compared to metals and boron, with boron being the most sluggish component. Consequently, boron plays a key role in determining the crystallization rate, which in turn influences the degree of amorphization.

D. Synthesis method of FeCoNiMoBO$_x$

Equimolar amounts of $Fe(NO_3)_3$, $Co(NO_3)_2$, $Ni(NO_3)_2$, and $(NH_4)_6Mo_7O_{24}$ (ammonium molybdate) were first prepared and dissolved in an equal volume of solvent to achieve a final concentration of 0.2 M, after which the solution was stored at 4 °C. Meanwhile, a 5 M $NaBH_4$ solution was prepared and refrigerated under the same conditions for 72 hours.

Subsequently, the metal salt solutions were combined in an ice bath, and a 5 M $NaBH_4$ solution, with twice the total volume of the metal salt solution, was rapidly added under vigorous stirring while maintaining the ice bath throughout the process. After reaction times of 3, 6, and 18 hours, three distinct catalysts, designated as Group-1, -2, and -3 FeCoNiMoBO$_x$, were obtained.

E. Catalytic descriptor calculation

The unoccupied d-band state parameter (λ_1) and the active d-band state parameter (λ_2) for Co ions are employed to characterize, respectively, the degree of unoccupied d-band states at active sites and the number of active states available for electron transfer. These parameters are essential for evaluating the oxygen evolution reaction (OER) performance of $FeCoNiMoBO_x$ catalysts with varying boron (B) content. Specifically, λ_1 and λ_2 are calculated by integrating the projected density of states (PDOS) corresponding to the relevant electronic bands, as follows:

$$\begin{aligned} \lambda_1 &= N_{\mathrm{Co}_{3d_{\mathrm{unoccupied}}}} + \frac{N_{\mathrm{Co}_{d_{x^2-y^2},d_{z^2}\,\mathrm{unoccupied}}}}{N_{\mathrm{O}_{2p_{\mathrm{unoccupied}}}}}, \\ \lambda_2 &= N_{\mathrm{Co}_{3d}} \times \frac{N_{\mathrm{Co}_{d_{x^2-y^2},d_{z^2}\,\mathrm{unoccupied}}}}{N_{\mathrm{O}_{2p_{\mathrm{unoccupied}}}}}, \end{aligned} \tag{S2}$$

where $N_{\mathrm{Co}_{3d}}$, $N_{\mathrm{Co}_{3d_{\mathrm{unoccupied}}}}$, $N_{\mathrm{Co}_{d_{x^2-y^2},d_{z^2}\,\mathrm{unoccupied}}}$, and $N_{\mathrm{O}_{2p_{\mathrm{unoccupied}}}}$ represent, respectively, the total number of states in the Co $3d$ band, the number of unoccupied states in the Co $3d$ band, the number of unoccupied states specifically within the Co $d_{x^2-y^2}$ and d_{z^2} orbitals, and the number of unoccupied states in the O $2p$ band. The parameter λ_1 quantifies the extent of unoccupied d-band states at Co active sites; higher λ_1 values indicate fewer electrons occupying the d-band and lower d-band electron energy levels, facilitating electron transfer from adsorbates to metal active sites and thereby reducing OER overpotential. Meanwhile, the parameter λ_2 quantifies the number of active d-band states at the Co site capable of participating in electron transfer interactions with the O $2p$ orbital under conditions of weak metal–oxygen interaction. Higher λ_2 values indicate a greater number of active states available for electron transfer, also leading to a reduction in OER overpotential.

S2 Supplementary Figures

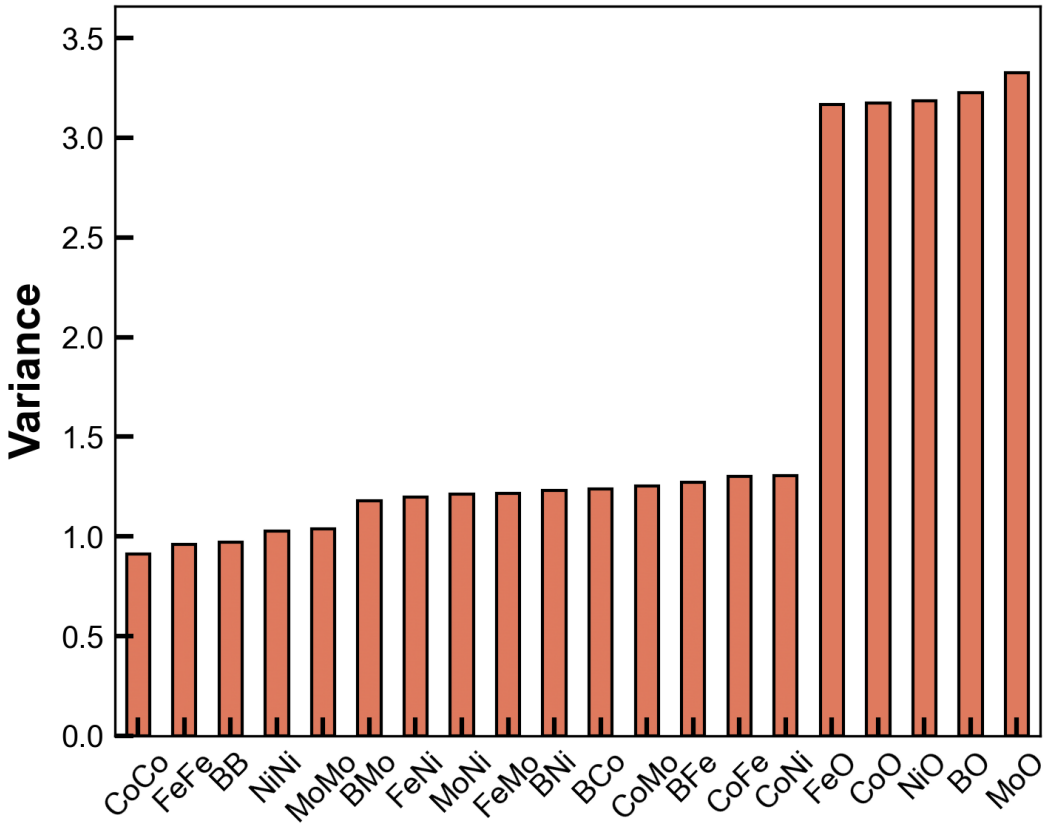

FIG. S1. **Variance-to-mean ratio of PDM across all energy ranges.**

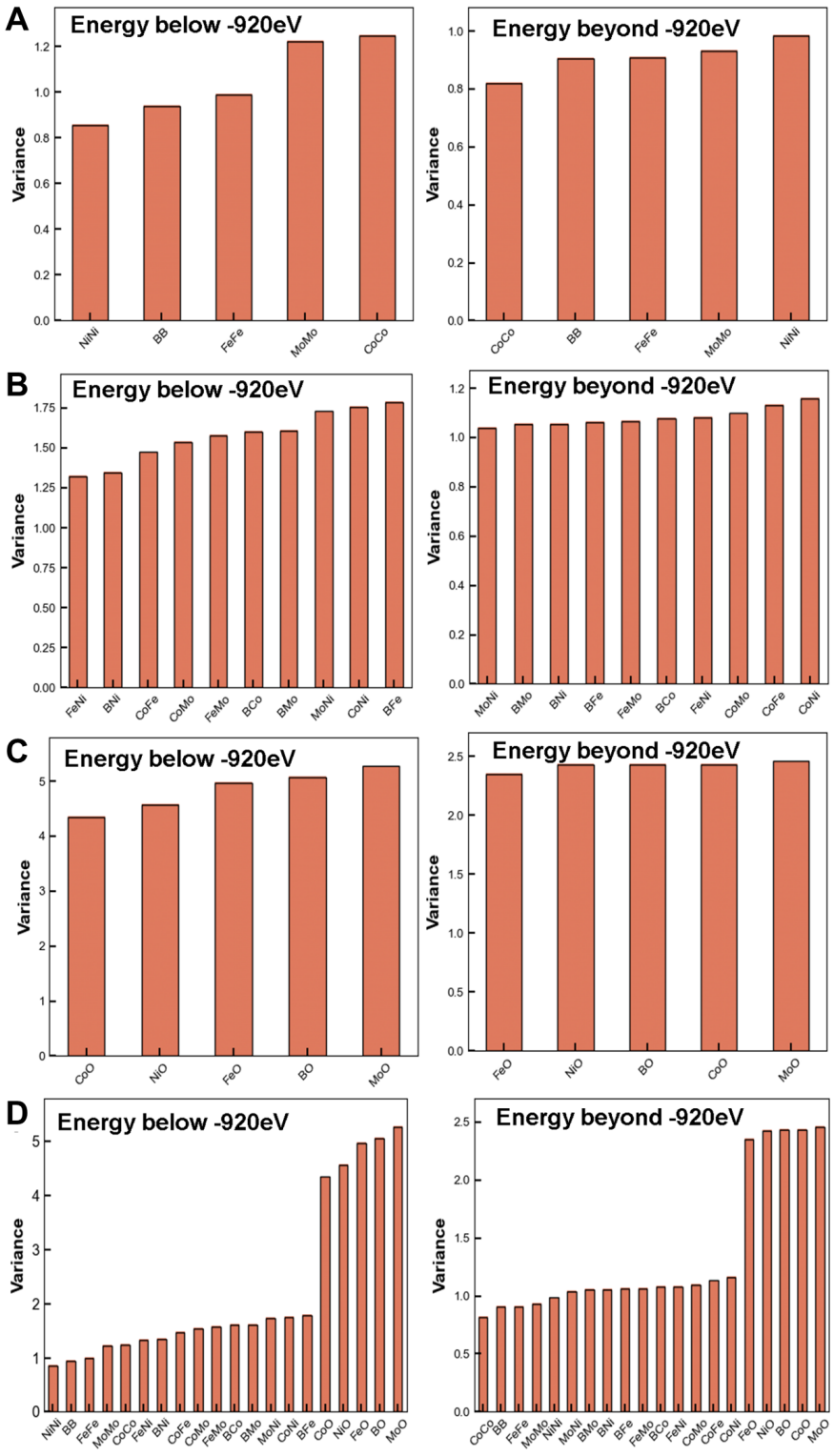

FIG. S2. **Normalized variance analysis of pair distributions.** (**A**) Variance of elemental pairs. (**B**) Variance of intermetallic pairs. (**C**) Variance of metal-oxygen pairs. (**D**) Variance of all elements in the pair distribution matrix. The variance is normalized by dividing it by the corresponding mean value.

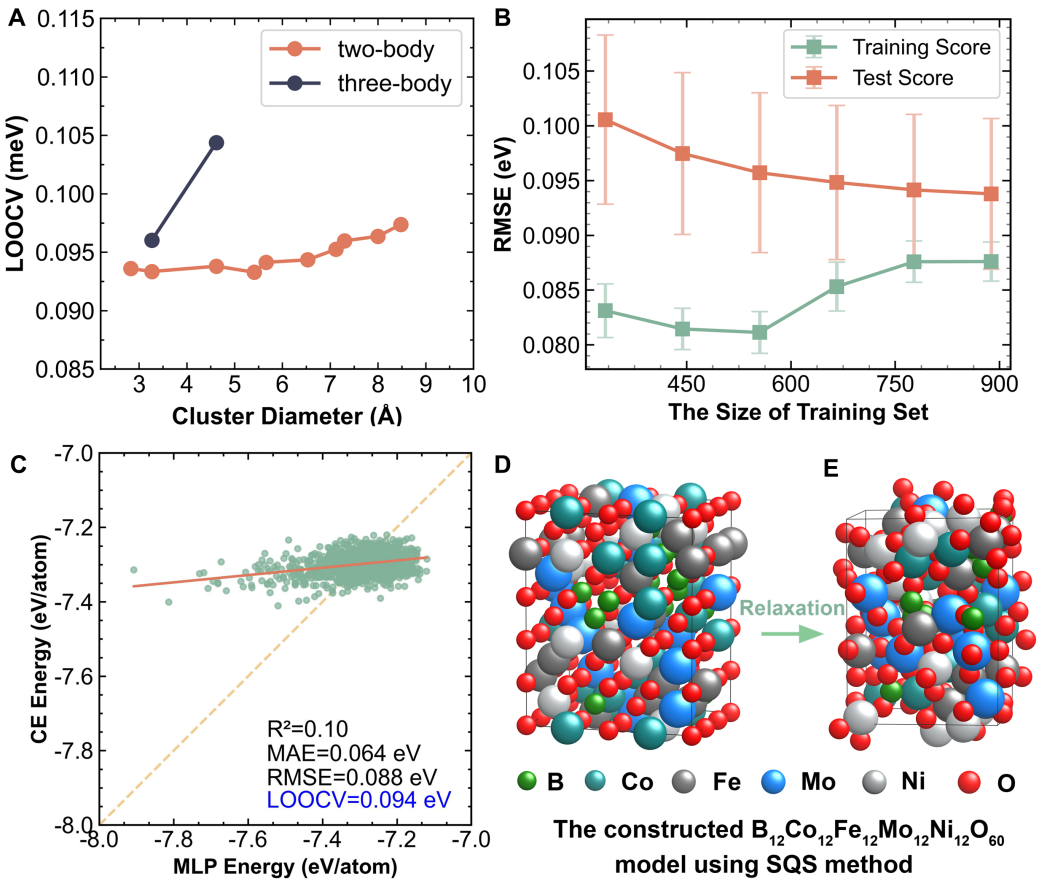

FIG. S3. **The fitting information of clusters expansion using ATAT program.** (**A**) The leave-one-out cross validation (LOOCV) scores for the test cluster diameters. All LOOCV scores exceed the acceptable values (0.02 eV) recommended by ATAT, nevertheless, the cluster corresponding to the lowest LOOCV score (a cutoff distance of 5.5 Å for two-body clusters) was selected for ECI fitting. (**B**) Learning curves for the selected model with least-squares fitting of ECIs. (**C**) Comparison between input energies obtained via MLP relaxation and the predicted energies from the CE model. (**D**–**E**) One of the states of SQS configuration before and after relaxation used for fitting the ECIs, with the amount of distortion annotated as 0.0128 by ATAT.

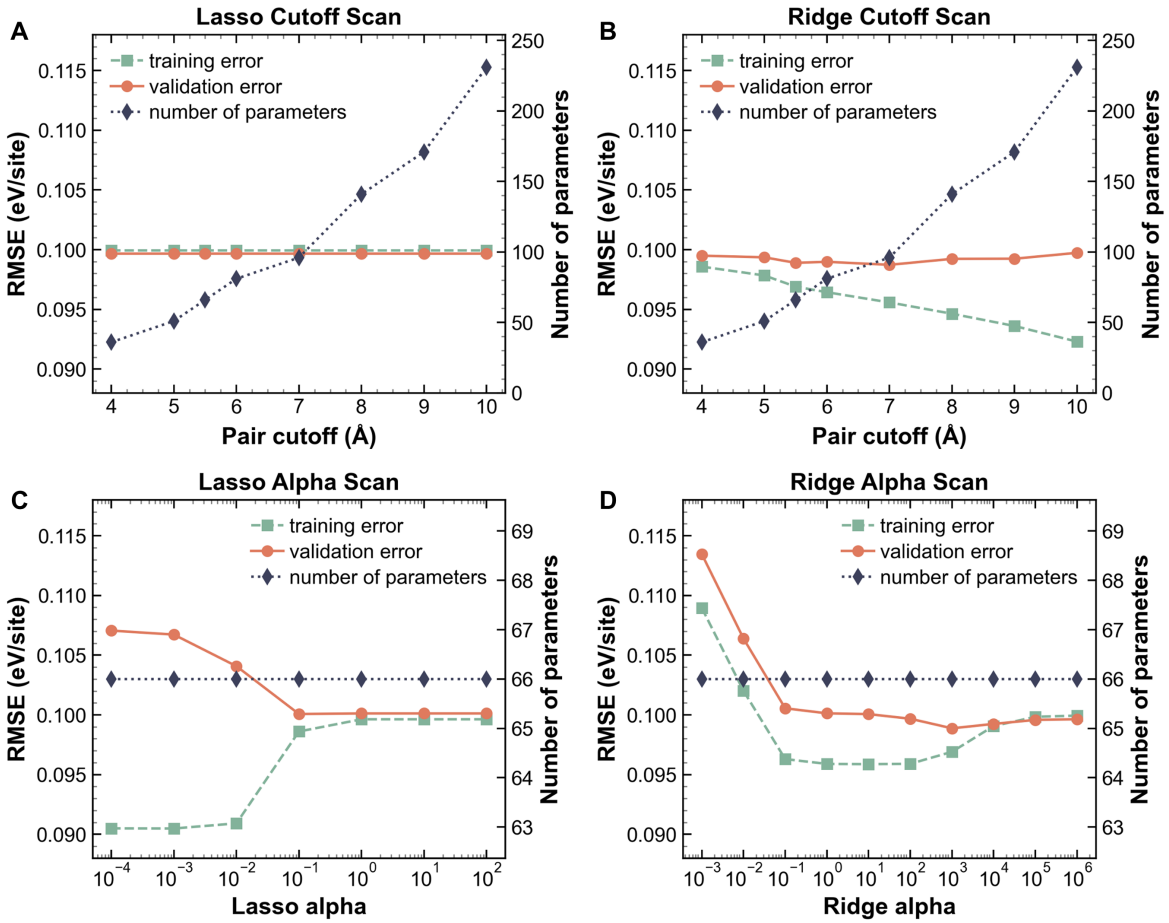

FIG. S4. **The cluster expansion fitting method using ICET package.** (**A**) The cluster diameter test of two-body (pair) clusters fitting with lasso method. (**B**) The cluster diameter test of two-body (pair) clusters fitting with ridge method. (**C**) The hyperparameter scan of lasso method. (**D**) The hyperparameter scan of ridge method.

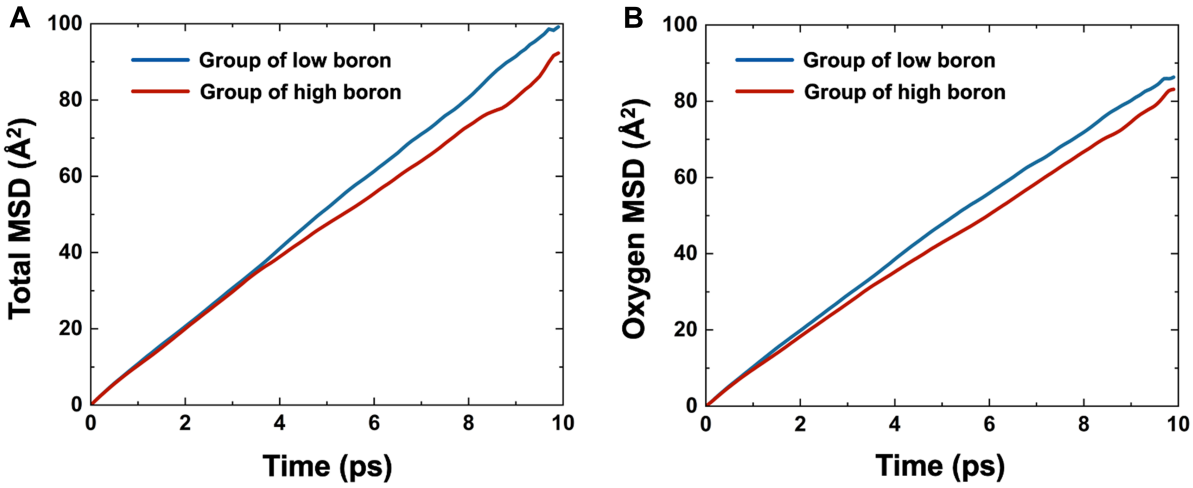

FIG. S5. **Diffusion rate analysis across groups with different boron contents.** **a** Total Mean Squared Displacement (MSD) of all elements. **b** MSD of oxygen atoms.

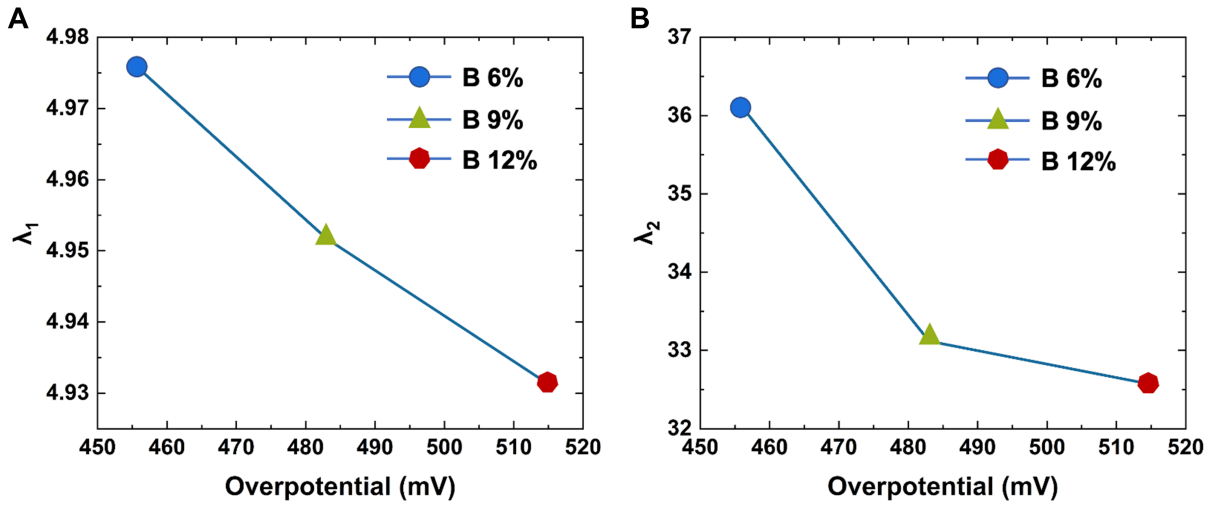

FIG. S6. **Catalytic descriptor calculation.** (**A**) Calculated λ_1 and (**B**) λ_2 values for Co in relation to experimentally measured OER overpotentials in $FeCoNiMoBO_x$ catalysts across three groups with varying boron (B) content (6%, 9%, and 12%). The calculation method is described in the recent study on multi-element oxides for OER performance.[2]

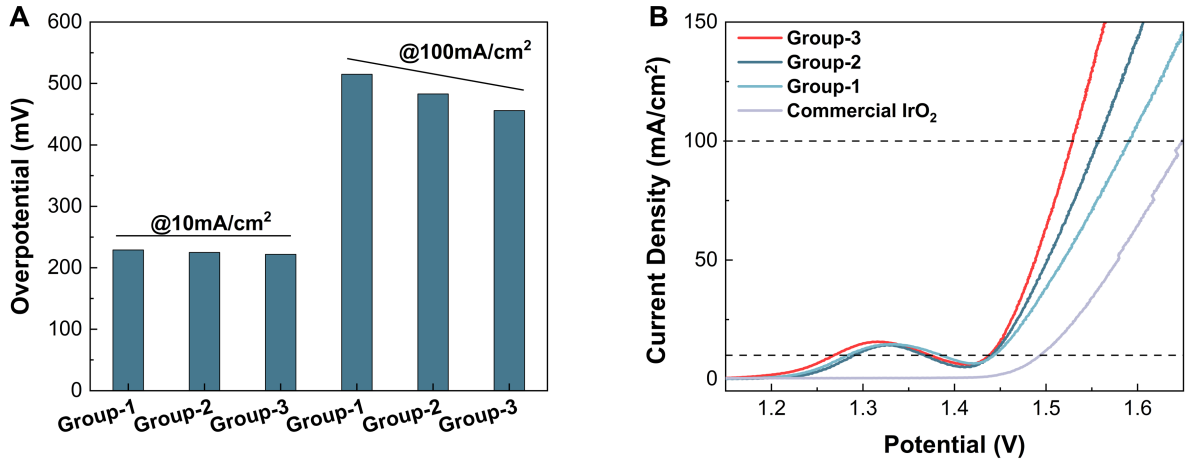

FIG. S7. **Catalytic performance.** (**A**) OER overpotentials across different groups at varying current densities. (**B**) Linear sweep voltammetry curves of Group-1, -2, and -3, compared with commercial IrO_2.

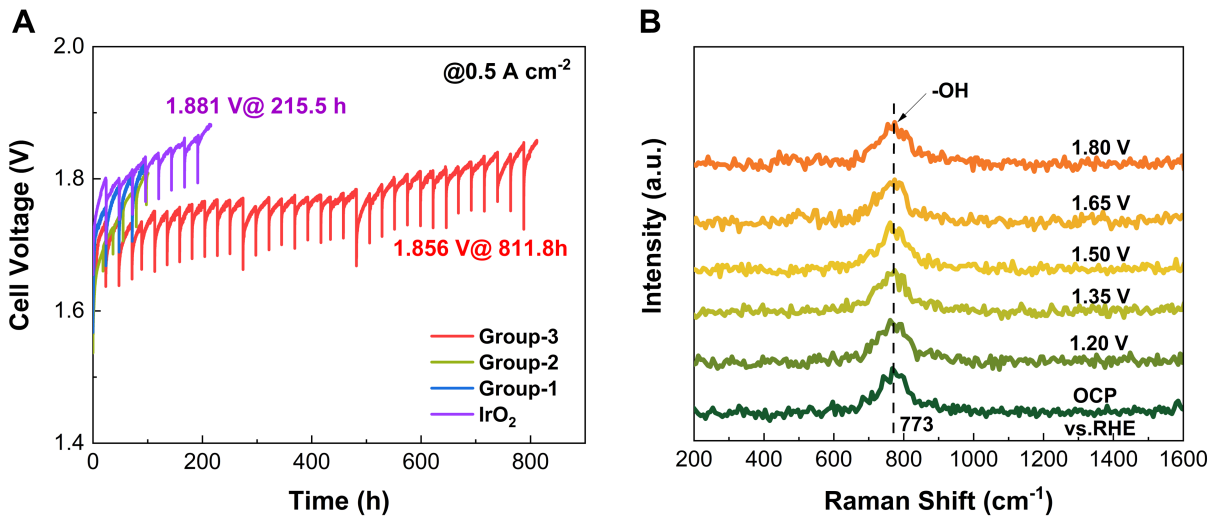

FIG. S8. **Catalytic stability.** (**A**) Stability test at 0.5 A/cm^2 using an anion exchange membrane (AEM) device for different groups, compared with IrO_2. (**B**) In-situ Raman spectra of $FeCoNiMoBO_3$ (Group-3).

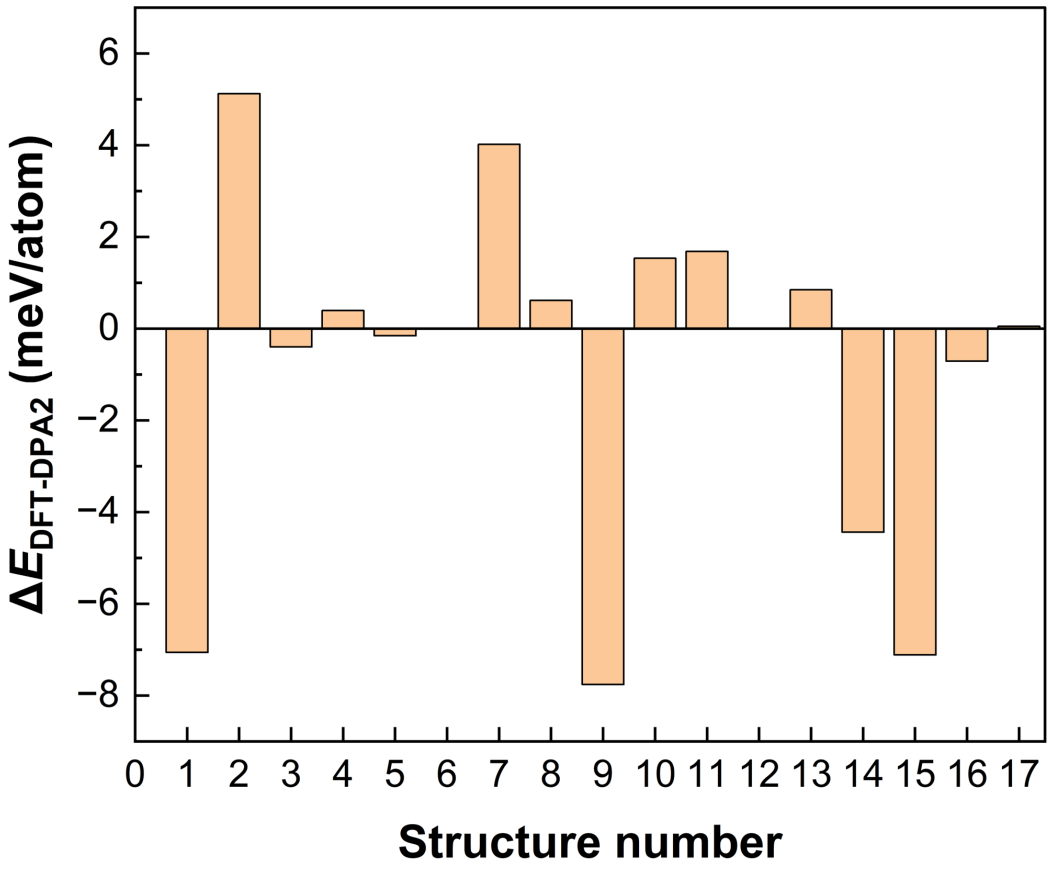

FIG. S9. **Accuracy analysis of DPA-2.** Compared the energy differences between DFT and DPA-2 for structures within different energy intervals to evaluate the accuracy of the MLP. The horizontal axis represents the number of structures, while the vertical axis shows the energy discrepancy between DFT and DPA-2 for each respective structure.

S3 Supplementary Tables

TABLE S1. **Hyperparameters of Cond-CDVAE model used in this work.** Each element type is embedded by a vector of length 50. MLP_{zc} is a multi-layer perceptron for concatenated latent vector and condition embedding vector. DimeNet++ [3, 4] and GemNet-dQ [5] are used as PGNN_{Enc} and PGNN_{Dec}, respectively.

Model	**Value**
Element type embedding	50
vectorized PDM dimension	197
MLP_{zc} number of layers	3
MLP_{zc} number of hidden channels	64
MLP_{L} number of layers	1
MLP_{L} number of hidden channels	256
PGNN_{Enc} number of blocks	4
PGNN_{Enc} number of hidden channels	128
PGNN_{Enc} interaction embedding size	128
PGNN_{Dec} number of blocks	4
PGNN_{Dec} number ofhidden channels	128
Loss weight $\lambda_{\mathbf{L}}$	10
Loss weight $\lambda_{\mathbf{X}}$	10
Loss weight β	0.01
Optimizer	**Value**
Optimizer type	Adam
Learning rate	1e-4
Learning rate scheduler	ReduceLROnPlateau
Scheduler patience (epoch)	30
Scheduler factor (epoch)	0.6
Minimal learning rate	1e-5
Data	**Value**
Batch size	128

TABLE S2. **Elemental compositions of catalysts estimated from ICP and element analysis.** Metallic contents were determined by ICP, and O contents were detected by difference subtraction of mass conservation.

Catalyst	Fe (mol %)	Co (mol %)	Ni (mol %)	Mo (mol %)	B (mol %)	O (mol %)
Group-1	8.74	8.23	8.26	6.93	5.87	61.98
Group-2	9.02	8.65	8.62	6.45	8.47	58.79
Group-3	10.36	10.03	9.94	7.23	11.68	50.76

References

[1] Ångqvist, M. *et al.* Icet – a python library for constructing and sampling alloy cluster expansions. *Adv. Theor. Simul.* **2**, 1900015 (2019).

[2] Fan, F. *et al.* Applicable descriptors under weak metal-oxygen d–p interaction for the oxygen evolution reaction. *Angew. Chem. Int. Ed.* e202419718 (2024).

[3] Gasteiger, J., Groß, J. & Günnemann, S. Directional message passing for molecular graphs. In *International Conference on Learning Representations* (ICLR, 2020).

[4] Gasteiger, J., Giri, S., Margraf, J. T. & Günnemann, S. Fast and uncertainty-aware directional message passing for non-equilibrium molecules. In *Advances in Neural Information Processing Systems* (NeurIPS, 2020).

[5] Gasteiger, J., Becker, F. & Günnemann, S. GemNet: Universal directional graph neural networks for molecules. In *Advances in Neural Information Processing Systems* (NeurIPS, 2021).